photonics

MDPI

Article

Design and Optimization of Silver Nanostructured Arrays in Plasmonic Metamaterials for Sensitive Imaging Applications

Koichi Okamoto [1,*], Daisuke Tanaka [2], Tetsuya Matsuyama [1], Kenji Wada [1], Yusuke Arima [3] and Kaoru Tamada [3,*]

[1] Department of Physics and Electronics, Osaka Metropolitan University, Osaka 599-8531, Japan
[2] Department of Electrical and Electronic Engineering, National Institute of Technology (KOSEN), Oita College, Oita 870-0152, Japan
[3] Institute for Materials Chemistry and Engineering, Kyushu University, Fukuoka 819-0395, Japan; arima@ms.ifoc.kyushu-u.ac.jp
* Correspondence: okamot@omu.ac.jp (K.O.); tamada@ms.ifoc.kyushu-u.ac.jp (K.T.)

Abstract: This paper delves into the strategic design and optimization of silver (Ag) nanostructured arrays within plasmonic metamaterials, targeting the enhancement of imaging sensitivity. Leveraging Finite-Difference Time-Domain (FDTD) simulations, our research rigorously compares various Ag nanostructured geometries, including nanospheres, nanocones, nanodisks, and nanocubes. The aim is to pinpoint configurations that significantly enhance electric field localization on the surfaces of nanostructures, a pivotal factor. The nanocube array exhibits superior field enhancement, particularly in narrow nanogaps, suggesting its suitability for high-sensitivity applications. Further exploration into nanocube arrays reveals the crucial role of nanogap size and spacer layer thickness in tuning the optical properties through the manipulation of Fabry–Pérot and mirror image modes in metal–insulator–metal (MIM) structures. By presenting a thorough analysis of these nanostructured arrays, the study not only contributes to our understanding of the fundamental principles governing plasmonic metamaterials but also provides a solid foundation for future innovation in highly sensitive imaging applications. It underscores the importance of nanostructure design and optimization in achieving significant improvements in the performance of plasmonic devices, marking a pivotal step forward in the field of nanophotonics and its application to sensitive imaging technologies.

Keywords: plasmonics; metamaterials; localized surface plasmon resonance; nanocube array; metal–insulator–metal; nanostructures on mirror

Citation: Okamoto, K.; Tanaka, D.; Matsuyama, T.; Wada, K.; Arima, Y.; Tamada, K. Design and Optimization of Silver Nanostructured Arrays in Plasmonic Metamaterials for Sensitive Imaging Applications. *Photonics* **2024**, *11*, 292. https://doi.org/10.3390/photonics11040292

Received: 11 March 2024
Revised: 18 March 2024
Accepted: 20 March 2024
Published: 24 March 2024

1. Introduction

Plasmonic metamaterials have emerged as a transformative technology in the field of optics and photonics, harnessing the power of surface plasmon (SP) resonances to manipulate light at the nanoscale [1–4]. These materials offer unprecedented control over light–matter interactions, enabling phenomena such as negative refraction [5,6], superlensing [7–9], and cloaking [10–12], which were once deemed theoretical. The fundamental principle behind plasmonic metamaterials involves the use of metal–dielectric structures to support SPs, facilitating light manipulation well below the diffraction limit of conventional optics. Among the various configurations of plasmonic metamaterials, metal–insulator–metal (MIM) structures stand out for their unique ability to confine and guide electromagnetic waves in ultra-compact dimensions [13–16]. This configuration not only enhances the local electromagnetic field but also allows for the engineering of the material's optical properties by adjusting the thickness of the dielectric layer and the type of metals used [17–19]. The versatility of MIM structures has led to their exploration in various applications, ranging from subwavelength waveguides and sensors to novel photonic devices. The application of plasmonic metamaterials, particularly MIM structures, in the realm of imaging represents a significant leap forward. By overcoming the diffraction limit,

these materials enable super-resolution imaging, allowing for the visualization of features much smaller than the wavelength of light [9,20–23]. Furthermore, vivid full-color development using plasmonic metamaterials based on the MIM structure has been reported, which is expected to be applied to flexible, tunable color printing technologies [24–29]. This capability has profound implications for medical diagnosis, where the enhanced resolution and contrast of plasmonic metamaterial-based imaging systems can facilitate the early detection of diseases at the cellular or even molecular level [30,31]. Furthermore, the sensitivity of plasmonic metamaterials to changes in the local refractive index makes them ideal candidates for label-free biosensing applications, providing a non-invasive means to detect and monitor biological markers in real-time [32,33]. The design and optimization of silver nanostructure array structures are the most important factors in advancing these applications. For example, to improve imaging sensitivity through surface-enhanced Raman scattering (SERS), various approaches have been utilized, including the application of graphene oxide on magnetron-sputtered silver (Ag) thin films [34], the creation of Ag nanowire arrays on paper via automated drawing methods [35], and the synthesis of various Ag-nanostructured substrates through physical vapor deposition and chemical synthetic routes [36], all aimed at the optimization of Ag-nanostructured array structures. Furthermore, the use of machine learning with deep neural networks has been explored for the design and optimization of comprehensive nanostructured array structures [37–39].

In the exploration of plasmonic metamaterials and their profound capabilities to manipulate light at the nanoscale, we have embarked on a comprehensive study to optimize the structural geometry of nanostructures for advanced imaging applications. Employing arrays of metal nanoparticles to manipulate localized SP modes presents a viable strategy. Notably, our recent investigations unveiled distinctive optical characteristics in three-dimensional stacked Ag nanosheets on metallic substrates [40,41]. The extinction spectrum displayed a bifurcation into dual peaks, a phenomenon absent when using transparent substrates. This optical behavior stems from a mode-splitting effect resulting from intense coupling. Consequently, Ag nanosheet constructs serve as effective plasmonic metamaterials. Leveraging this architecture, we have documented several practical applications, including colorimetric biosensing [42], detection of photocatalytic reactions [43], augmentation of fluorescence imaging [44], and achieving ultrahigh-resolution imaging capabilities [45]. Our primary objective is to understand and enhance the interaction of light with two-dimensional nano-array configurations, which are pivotal in achieving high-resolution imaging at scales previously unattainable. The path to this understanding involves the meticulous design and simulation of various nanostructures, such as nanospheres, nanocones, nanodisks, and nanocubes, and the examination of their electric field distributions. We employ Finite-Difference Time-Domain (FDTD) simulations to unravel the complex interplay between the electric field and the nanostructures, thereby shedding light on the potential for 'hot spots' or areas of intense electric field localization [46–48]. These hot spots are crucial for enhancing the optical response of the materials and for the development of next-generation sensors and imaging devices. Our simulations reveal that the field enhancement is dependent on the geometric arrangement and the physical dimensions of the nanostructures, particularly the gap size between them. By manipulating these parameters, we can tune the localized plasmon resonances and control the electric field distribution. This tunability offers a pathway to precisely control the resonance spectra of the nanostructures, thus enabling the manipulation of their optical properties for specific applications.

Plasmonic metamaterials have been used for many applications across a wide range of fields, and various nanostructures have been devised for this purpose. Compared to many of these previous reports, the structures designed and optimized in this study are unique in that they are specialized, two-dimensional array structures that can be fabricated by the self-assembly of nanostructures without requiring top-down nanofabrication techniques such as electron beam lithography. This makes it both easy and convenient to fabricate large-area structures and, thus, it holds extremely high potential for practical use. Furthermore, we

are considering a two-dimensional array structure on a metal substrate by combining it with the MIM structure to elucidate and control the interaction of plasmon modes, enabling the flexible control of both the intensity of the localized electric field and the resonance wavelength. This novel strategy, scarcely reported in the existing literature, is introduced for the first time in this study. The findings of this study extend beyond theoretical simulations to practical applications, which can be achieved by fabricating optimized structures using self-assembly techniques. This work lays the groundwork for a new class of plasmonic metamaterials with tailored optical characteristics. By elucidating the mechanisms that govern the interaction of light with nanostructures, we pave the way for innovative applications in high-sensitivity imaging and beyond. The findings from this research hold promise for advancing the field of plasmonics, with the potential to revolutionize the capabilities of optical devices and enhance our understanding of light–matter interactions at the nanoscale.

2. Methods

Details of the FDTD simulations performed using a commercially available software (Poynting for Optics, Fujitsu, Japan) have been described in previous reports [40–44]. A nonuniform mesh was used with a grid size of 0.5–5 nm. Periodic and absorption boundary conditions were applied in the X and Y directions, as well as in the Z direction, respectively. A pulsed light composed of a differential Gaussian function with a pulse width of 0.5 fs and an electric field of 1 V/m was irradiated under an X-polarized source to calculate the electric field distributions and the resonance spectra. The peak position of the excitation pulse spectrum was approximately 600 THz (wavelength: 500 nm). The refractive index of the glass was set at 1.5 without dispersion. The dielectric function of Ag was approximated using the Drude formula, based on the values reported by Johnson and Christy [49]. Square lattices were used as the array structure to easily create repeating units. Simulation results confirmed that the effect of the hexagonal lattice/square lattice is negligibly small in the reflectance and transmission spectra. Extinction coefficient spectra were obtained by converting from reflectance and transmittance spectra for each structure.

3. Results and Discussions

3.1. Nanostructure Geometries for Optimal Electric Field Localization

Firstly, we delved into the comparative analysis of nanosphere, nanocone, and nanodisk geometries to form two-dimensional sheet configurations. Figure 1a displays the simulated models of these nanostructures, alongside the spatial distribution of the electric field on the structures' surface when arranged in a two-dimensional array. Notably, the edge of each structure exhibits intense electric field localizations, commonly referred to as 'hot spots', which is a defining characteristic of two-dimensional nano-array configurations and is critical in determining the functional efficacy of these hot spots [46–48].

Figure 1b further presents the spatial distribution of the electric field around the nanostructures in a cross-sectional view, clearly identifying the formation of hot spots within the nano gaps of the structures. Figure 1c offers the extinction spectra calculated from the transmission spectra for arrays of nanosphere, nanocone, and nanodisk sheets. The incident light is oriented perpendicularly to the sheet, with its electric field oscillating horizontally as depicted in the figure. These spectra reveal sharp absorption peaks, presumably originating from localized SP resonances (LSPRs) across all nanoparticle sheets. A singular peak at 435 nm for the nanosphere sheet, double peaks at 372 nm and 501 nm for the nanocone sheet, and a peak at 477 nm for the nanodisk sheet are observed, with the peak magnitudes following the order of nanodisk > nanosphere > nanocone. In Figure 1b, the nanosphere sheet demonstrates the most significant enhanced electric field within the closest gaps. However, the electric field seeping onto the substrate surface is minimal, indicating that most of the enhancement is concentrated within the gaps. The nanodisk sheet, in contrast, showcases an enhanced electric field between the discs, with strong optical electric fields

arising in the near-field regions on the top and bottom surfaces. This indicates that the enhanced electric field of the nanodisk sheet is the most substantial at the sheet surface.

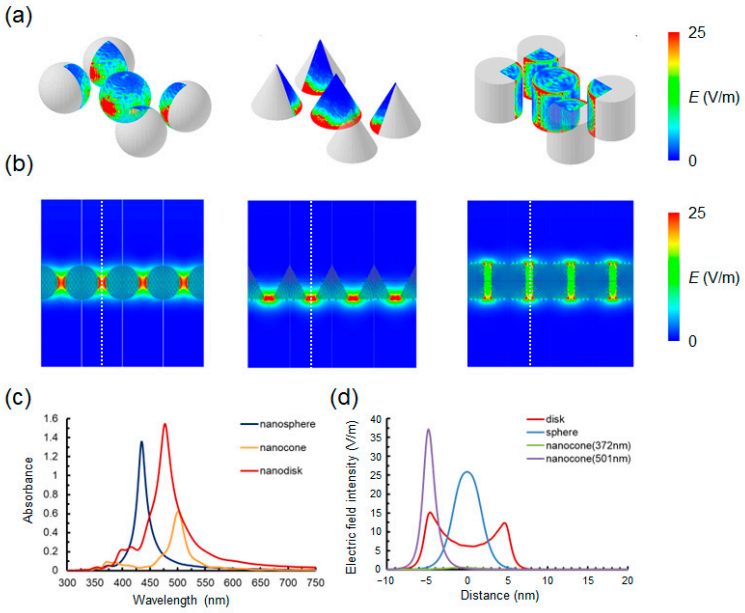

Figure 1. (**a**) Simulated models of nanospheres, nanocones, and nanodisks and the spatial distribution of the electric field on the surface when arranged in a two-dimensional array. (**b**) Cross-sectional view of the electric field distribution around the nanostructures, illustrating the formation of hot spots within the nano gaps. (**c**) Extinction spectra for arrays of nanosphere, nanocone, and nanodisk sheets, showing the distinct LPR-derived absorption peaks. (**d**) The electric optical field intensity distribution between the gaps of each nanostructure.

Figure 1d isolates the electric field distribution between the gaps of each structure, as delineated by the dashed lines in Figure 1b. The nanosphere sheet exhibits a robust enhanced electric field between the nearest gaps; however, the electric field emerging on the sheet surface is minimal, implying that most of the enhanced field remains buried. For the nanocone sheet, a strong enhancement field arises between the edges on the bottom surface of the disk, and this enhancement, similar to that of the nanosphere sheet, is buried with respect to the sheet's upper surface. The nanocone's enhancement field could be utilized if the top and bottom surfaces were inverted. The nanodisk sheet, however, exhibits enhancement fields between the disks, leading to strong optical electric fields in the near-field regions on the top and bottom surfaces. Although the peak value of the partial electric field in the hot spots of the nanocone is stronger than that of the nanodisk, the nanodisk has two hot spots on both the upper and lower sides. Consequently, the field enhancement effect of the nanodisk sheet is the strongest among the three structures, accounting for the strongest peak in the resonance spectrum, as shown in Figure 1c. This conclusion posits that for the utilization of the surface electric field enhancement effect, the nanodisk structure is the most suitable.

Figure 2a presents the cross-sectional view of electric field distribution for nanodisk sheets with varying gap distances. Each Ag nanodisk possesses a diameter and height of 10 nm. It is observed that as the gap distance narrows, the enhanced electric field increases, but is primarily localized near the nanosheet surface due to pronounced light confinement effects. For instance, the magnitude of the enhanced electric field at a position 5 nm above the nanosheet is in the order of 5 nm > 2 nm > 1 nm is inversely related to the surface enhancement field strength. These findings suggest that the leakage length from the nanosheet can be controlled by the gap length, implying a tunable interaction interface for biosensing applications, such as in cell–sheet contact interfaces for microscopic substrates. Figure 2b,c display the dependency of the maximum localized electric field

and peak wavelength on the nanogap, respectively. The enhancement effect dramatically increases for gaps shorter than 3 nm, with the peak wavelength showing a gradual redshift as the gap decreases. This phenomenon is well known as SP coupling in the narrow confines between two metallic structures, referred to as the nanogap mode. The robust electric field enhancement and tunability provided by this nanogap mode are among the most significant advantages of the nanosheet structures. Moreover, the interaction of this nanogap mode results in new optical properties across the entire structure due to the coherent interaction of electric field oscillations within the nanostructures, making it a vital element for plasmonic metamaterials.

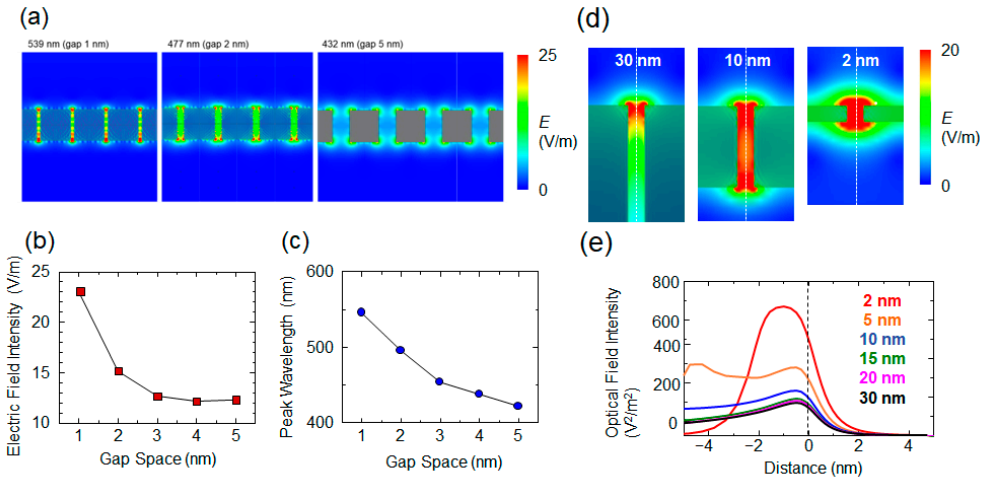

Figure 2. (**a**) Electric field distribution cross-sections for nanodisk sheets with different gap spaces, showing increased field enhancement with narrower gaps. (**b**) Electric field intensity dependency on the gap space. (**c**) Peak wavelength shift as a function of gap space. (**d**) Dependency of electric field distribution on the nanodisk height, showing stronger coupling with thinner disks. (**e**) Optical field intensity profiles within nanogaps with various gap distances.

Figure 2d illustrates the dependency of the electric field distribution on the nanodisk height for nanodisks of 10 nm in diameter and with varied gaps. The disk thickness is reduced from 30 nm to 2 nm, keeping the gap fixed at 2 nm. As the disk becomes thinner, the electric fields above and below the sheet couple more strongly and the field permeates more uniformly across the surface, suggesting that a thinner disk is required for applications that necessitate stronger electric fields. Particularly, the 2 nm nanodisk exhibits an extremely strong enhanced electric field. Figure 2e shows the line profile of the optical intensities inside the nanogap with various disk thicknesses. It was clearly shown that the optical fields on the top and bottom of the sheet combine and become stronger as the disk thickness becomes thinner, and it was also shown that the electric field seeps out over the entire surface. This result suggests that the disk thickness should be reduced when a stronger electric field is required. In particular, a very strong enhanced electric field was achieved for the 2 nm height of the nanodisk.

3.2. Optimization of Two-Dimensional Nano-Array Structures

In this study, we successfully optimized the shape of nanostructures that make up two-dimensional nano-arrays for efficient light confinement and high-resolution imaging applications. We then considered effective structures for the actual fabrication of two-dimensional nano-arrays. Although electron beam lithography can fabricate any shape [24–29], we advocate for self-organization methods that allow for the simple and inexpensive creation of large-area, two-dimensional array structures. Various shapes of two-dimensional nano-array structures have been created by self-organization [50–54]. However, as previously calculated, utilizing plasmon coupling modes that occur in nanogaps is essential. In particular, for a 2 nm thick nanodisk structure, setting the gap to 2 nm

is ideal. In disk array structures, the nanogap region formed between adjacent disks is narrow, making it difficult to reduce the thickness and nanogap to 2 nm. When considering the horizontal expansion of the area where nanogaps form in a broader region than the spherical shape, the nanocube structure can encompass a larger area of nanogaps than the nanodisk structure. Indeed, two-dimensional array structures of Ag nanocubes have been reported to be fabricated using various methods, with the length of one side ranging from 10 nm to 200 nm, and the gap spacing controllable in the several nm range or in the tens of nm range if an Ag/dielectric core–shell structure is used. [55–59]. Thus, we consider a two-dimensional array structure of a 30 nm Ag nanocube and, for comparison, a disk structure with a diameter of 30 nm and a height of 30 nm. We present the results of FDTD simulations for nanodisk and nanocube structures arranged in a square array with a 5 nm nanogap in Figure 3.

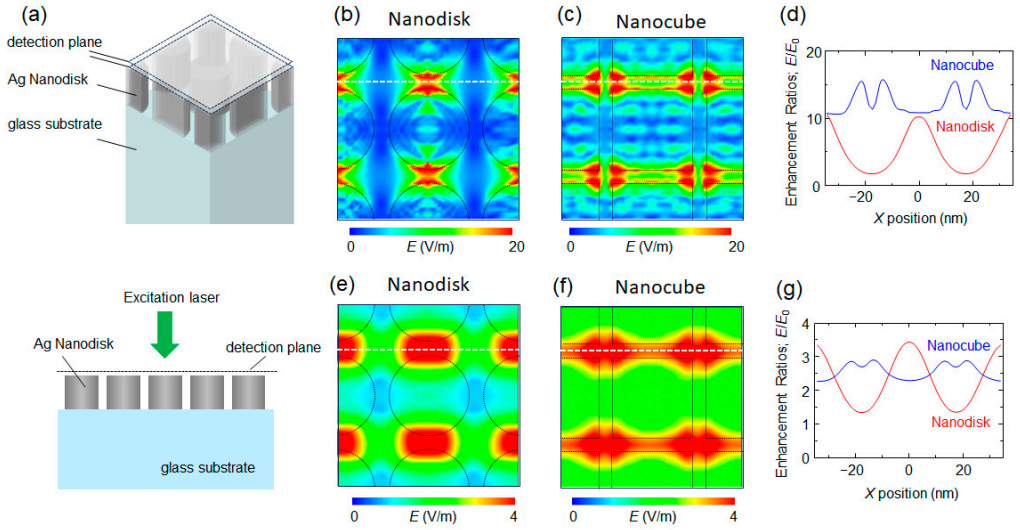

Figure 3. FDTD simulation results of two-dimensional arrays of nanodisk and nanocube structures with a nanogap of 5 nm. (**a**) Schematic of the simulation setup with Ag nanostructures on a glass substrate and an excitation laser irradiating from above. Electric field distribution at a 500 nm wavelength, 1 nm above the nanodisk (**b**) and nanocube (**c**) arrays, respectively. (**d**) Line profiles of field enhancement ratios for both structures. Further electric field distributions at a 500 nm wavelength of the nanodisk (**e**) and nanocube (**f**) arrays. (**g**) line profiles of enhancement at a detection plane 5 nm above.

Figure 3a depicts the model used for calculations, with Ag nanostructures arrayed on a glass substrate and irradiated from above to determine the spatial distribution of the electric field strength confined within the nanostructures at detection planes 1 nm and 5 nm above the nanostructures. Figure 3b,c show the electric field distributions at a 500 nm wavelength at the detection surface, 1 nm from the top end of the nanodisk and nanocube arrays, respectively. The line profiles of field enhancement compared with the scenario without nanostructures along the white dotted line are shown in Figure 3d. Similarly, Figure 3e–g show the electric field distributions and the line profiles of field enhancement on the detection surface 5 nm from the top end of the nanodisk and nanocube arrays. In the nanodisk, the enhanced electric field due to plasmon coupling localized in the nanogap is concentrated at one point; whereas, in the nanocube, it is distributed along a line. In particular, Figure 3g shows that near the hotspot in the nanodisk, an enhanced electric field of nearly three times is obtained, but in other areas, the field enhancement degree drops close to one, indicating regions where the field is not enhanced. Conversely, the nanocube shows a consistent two to three times enhancement along the line profile. Although this calculation is limited to polarization in the X-direction, using an unpolarized light source would result in only point-like enhancement spots in the nanodisk, while in

the nanocube, a mesh-like pattern of enhancement spots is obtained, suggesting a structure more suited to high-sensitivity imaging. Furthermore, the two-dimensional array structure of Ag nanocubes with a few nm gaps has already been fabricated by self-organization and, thus, we intend to further optimize this structure as a base.

3.3. Plasmonic Metamaterials Using MIM Structures with Nanocube Arrays

Having optimized the lateral two-dimensional array structures for high-sensitivity imaging, we will now consider optimization of the vertical structure. One approach is the multilayering of nano-array structures to create three-dimensional metamaterials, enabling light confinement in three dimensions [41]. However, even with electron beam lithography or self-organization, fabricating multilayer nano metal array structures is challenging. We have recently succeeded in vertically confining light by fabricating metallic nanostructures on metal substrates and exploiting their plasmon coupling modes. By fabricating metallic nano-hemispheres on a metal substrate through a dielectric spacer layer, we have reported an even stronger optical confinement and the ability to increase, sharpen, and control the resonance spectral peak, depending on the thickness of the dielectric spacer layer [60]. By changing the metal species and size of such a Nano-Hemisphere on Mirror (NHoM) structure, the resonance peak can be flexibly controlled over a wide wavelength range from deep UV to near IR wavelengths by changing the thickness of the dielectric spacer layer [61,62]. Similar metal Nanostructures on Mirror (NSoM) structures have been reported, where the resonant wavelength is controlled by the thickness of the spacer layer [63–67]. Most are explained by the interaction with the Fabry–Pérot (FP) mode in an MIM structure, where the resonant wavelength redshifts as the spacer layer thickens. Conversely, our proposed NHoM structure, while similar to MIM structures, exhibits an opposite dependence on the spacer layer thickness. This is due to the LSPR-enhanced electric field distribution in the metal nanostructures, which splits the peak when coupled with the mirror image mode of the metal substrate. As the spacer layer thins, the real and mirror image distances decrease and the coupling strengthens, widening the split and causing the peak that appears at longer wavelengths to redshift. Thus, in such an NSoM structure, the dependence of the resonance peak splitting/shift on the thickness of the spacer layer shows the opposite behavior when coupling with the mirror image mode occurs, as in our reported NHoM structure, or when coupling with the FP mode occurs, as in the MIM structure. The details of which contribution dominates the splitting/shifting of resonance peaks in the NSoM structure, coupling to the mirror image or coupling to the FP mode, and what conditions determine the contribution are still unclear. Therefore, we calculated the resonance spectra of the most promising two-dimensional metal nanosheet structure, nanocubes, when placed on a metal substrate to form an NSoM structure and investigated the mechanism of mode coupling and the controllability of resonance wavelengths.

Figure 4 shows the calculated reflection and transmission spectra for various Ag nanocube models. Figure 4a shows the result of calculating the Ag nanocube array structure as a virtual dielectric thin film with a strong interaction with uniform light without any structure by using the effective medium approximation. Such an effective medium approximation is often used for metal–dielectric composite materials and is obtained by optimizing the parameters of the Lorentz function to reproduce the reflection and transmission spectra obtained experimentally. To obtain the reflection and transmission spectra in Figure 4a, the optical properties were estimated by optimizing the experimental results of the reflection and transmission spectra reported for Ag nanocube arrays [60]. The obtained parameters for instantaneous dielectric constant (ε_∞), plasma angular frequency (ω_p), natural angular frequency (ω_0), and damping factor (γ) are 5, 6.6×10^{15} [rad/s], 3.0×10^{15} [rad/s], and 8.0×10^{14} [rad/s], respectively. Since the nanocubes are 30 nm on a side, the thickness of the effective medium is also assumed to be 30 nm. Natural materials with such spectra at a mere thickness of 30 nm are nonexistent, highlighting the extraordinary plasmonic metamaterial interaction with light. Figure 4b,c show the spectra for 30 nm and 50 nm Ag

nanocubes arranged far apart to eliminate interaction, both displaying an LSPR resonance peak near 500 nm. The effective medium approximation in Figure 4a assumes an interaction between particles, hence the peak is at a shorter wavelength than in Figure 4b, where there is no plasmonic interaction. In Figure 4c, the larger particles result in a larger peak slightly shifted to longer wavelengths. Considering a 30 nm Ag nanocube array structure, Figure 4d,e depict structures with nanogaps of 10 nm and 5 nm, respectively. As the nanogap decreases, the electric field enhancement and interaction strengthen, increasing the reflection and transmission peaks and causing a redshift. In particular, the 5 nm gap in Figure 4e closely replicates the experimental reflection and transmission peaks, suggesting this is the closest to the actual optical properties of the nanocube array structure.

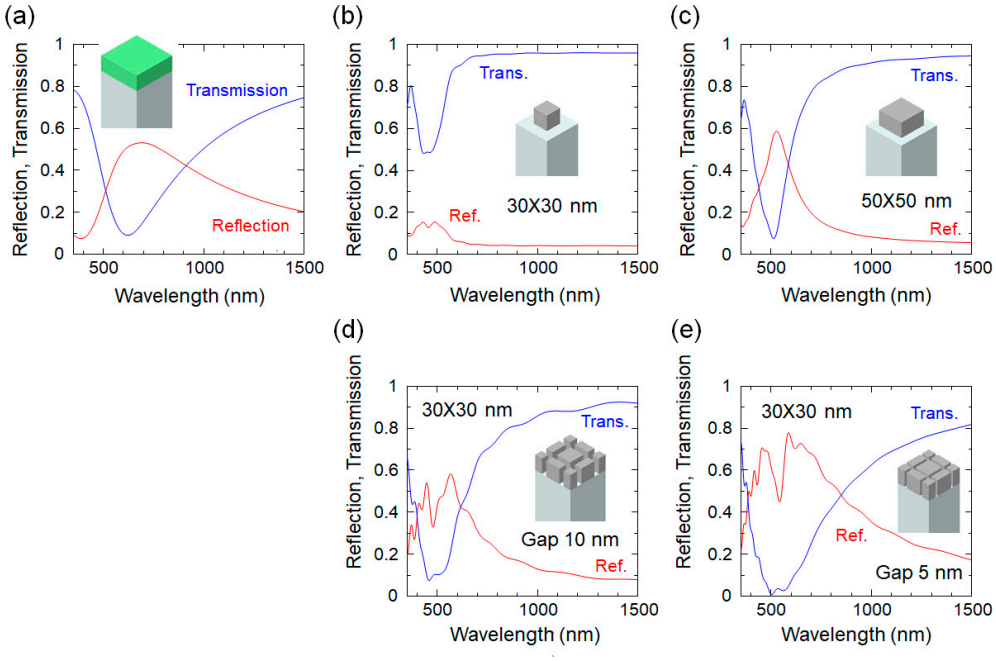

Figure 4. Reflection and transmission spectra calculated using the FDTD simulations for effective medium approximation model on Ag substrate (**a**), nanostructure/spacer/metal substrate models with isolated 30 nm (**b**) and 50 nm (**c**) Ag nanocubes, and nanostructure/spacer/metal substrate models with Ag nanocube array structure with 10 nm gaps (**d**) and 5 nm gaps (**e**).

We then proceeded to construct a model of the metal nanostructure/spacer/metal substrate, i.e., NSoM structure and created extinction spectra from the reflection and transmission spectra to examine the dependence on the spacer layer's thickness, as shown in Figure 5. In all cases, two peaks are present, which are thought to be due to the coupling with either the FP mode or the mirror image mode, or a mixture of both. Figure 6 plots the peak wavelengths against the spacer thickness. Particularly, we focus on the long-wavelength mode's spacer layer thickness dependence, which is prominent. In the model using an effective medium approximation shown in Figures 5a and 6a, the peak wavelength redshifts with increasing spacer thickness. This suggests a dominance of resonance with the FP mode, indicating that the effective medium in this case has metallic-like properties, forming a type of MIM structure. In contrast, for the case of the 30 nm nanocube with no interaction in Figures 5b and 6b, the opposite dependency is shown, with the peaks that were splitting approaching a single value as the spacer thickness increases. Similarly, for the 50 nm nanocube with no interaction in Figures 5c and 6c, the same trend is observed and as the spacer thickness increases, the peaks approach each other, causing the long mode to blueshift. However, since the splitting width converges to a constant value with increasing spacer thickness and does not approach any closer, there may be a contribution from resonance with the FP mode.

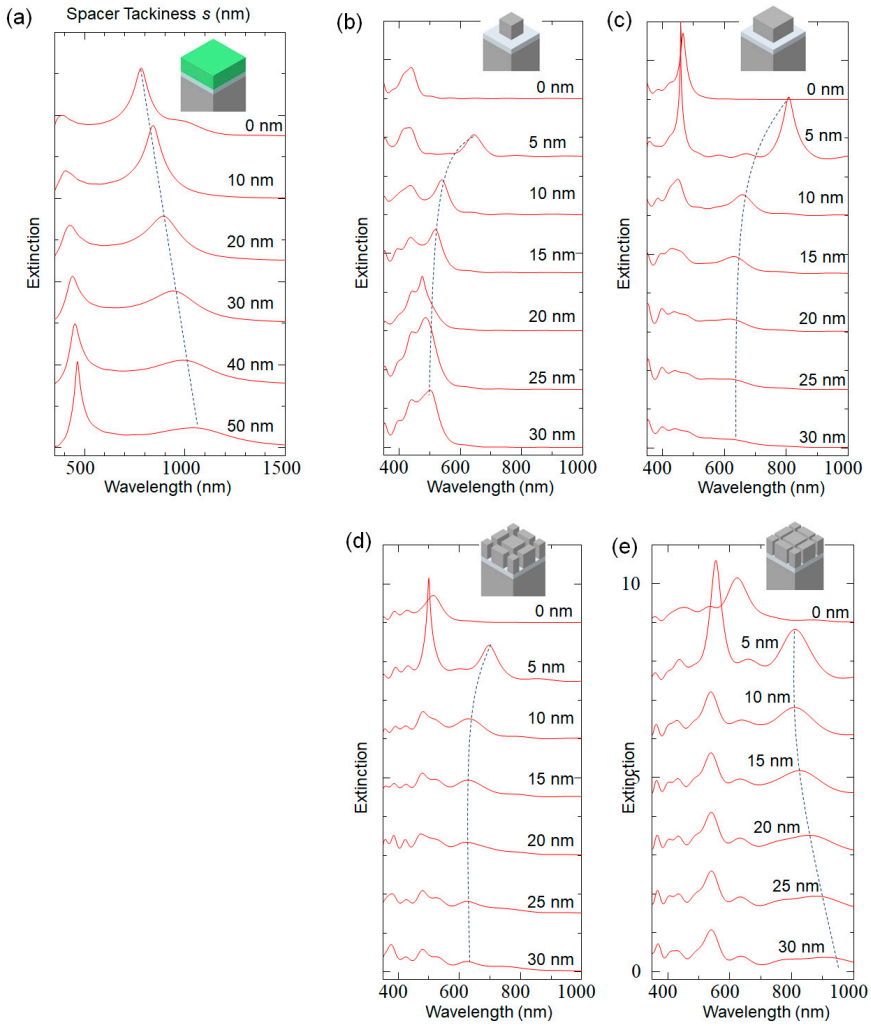

Figure 5. Extinction spectra demonstrating the dependency on spacer thickness for effective medium approximation model on Ag substrate (**a**), nanostructure/spacer/metal substrate models with isolated 30 nm (**b**) and 50 nm (**c**) Ag nanocubes, and nanostructure/spacer/metal substrate models with Ag nanocube array structure with 10 nm gaps (**d**) and 5 nm gap (**e**).

For the case with interactions between the nanostructures, for a nanogap of 10 nm shown in Figures 5d and 6d, the peak of the long mode redshifts slightly with spacer thickness, but then maintains a constant value. This could indicate that both resonances with the FP mode and mirror image mode are contributing, neutralizing each other's shifts to maintain a constant peak, wavelength, and splitting width. In the case of a nanogap of 5 nm shown in Figures 5e and 6e, a redshift occurs with increasing spacer thickness, similar to Figures 5a and 6a, suggesting that when the nanogap is 5 nm, the interactions between the nanostructures are stronger and the electric field application to light is more coherently integrated, resulting in a similar outcome to the effective medium approximation. This suggests that for a nanocube array structure with a nanogap of 5 nm, coupling with the FP mode becomes dominant when formed into an MIM structure. Thus, the resonance with the FP mode and the resonance based on the mirror image mode have different mechanisms, exhibiting opposite spacer layer dependencies, and which mechanism becomes dominant depends on the strength of the interaction between the metal nanostructures, which, in this case, varies with the size of the nanogap.

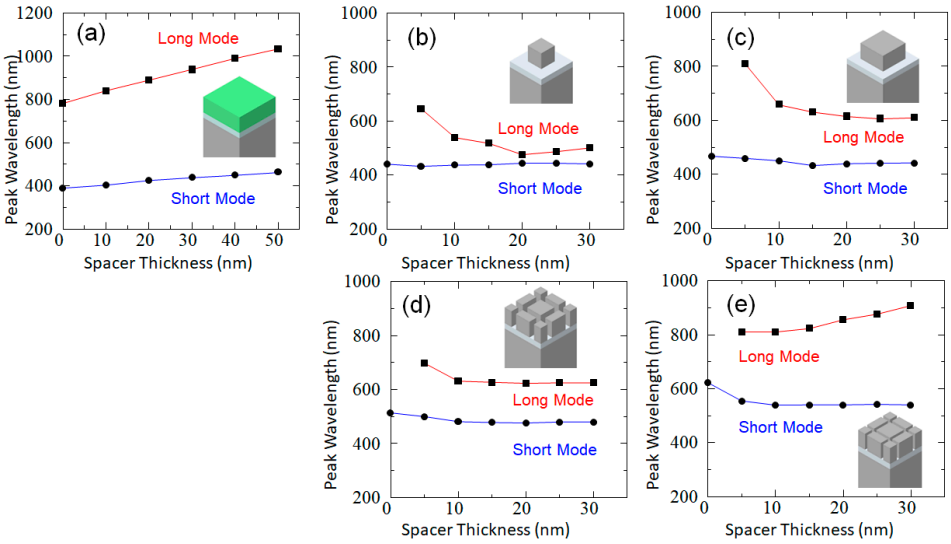

Figure 6. Plots of peak wavelengths with short and long modes as a function of spacer thickness for effective medium approximation model on Ag substrate (**a**), nanostructure/spacer/metal substrate models with isolated 30 nm (**b**) and 50 nm (**c**) Ag nanocubes, and nanostructure/spacer/metal substrate models with Ag nanocube array structure with 10 nm gaps (**d**) and 5 nm gap (**e**).

Next, we elaborate on the distinct mechanisms of the two modes and their resonance wavelength control based on this difference, along with their applications in high-sensitivity imaging. Figure 7a examines the electric field enhancement ratios on the glass substrate for both the short and long modes of the 30 nm side nanocube interacting at a 5 nm nanogap and in the absence of interaction. In both scenarios, a greater field enhancement than what would be expected from mere reflection off the glass substrate is achieved. Additionally, there is a dependency on the spacer thickness; for the FP mode-based case, the field enhancement slightly decreases as the spacer thickness and mode length increase. Conversely, for interactions with the mirror image mode, the degree to which the oscillations of the electric field neutralize each other and form a dark mode varies, thus altering the resonance's Q value, suggesting that there may be a maximum value at a certain spacer thickness.

Figure 7b,c depict the distribution of the X-polarized localized electric field around the nanocube side for the case of interaction at a 5 nm nanogap and for the case of no interaction, respectively. In Figure 7b, all electric field distributions are in phase, whereas in Figure 7c, they are divided into modes with different phases within the nanostructure. In Figure 7b, the mirror image mode is not pronounced, but in Figure 7c, interactions with the mirror image mode are evident. This determines which mode becomes dominant; interaction with the mirror image mode requires a mode of the localized electric field distributed within the nanostructure, and an opposing mirror image mode forms to neutralize it. However, for the FP mode, the distribution of the electric field is coherently integrated within the nanostructure, so no counteracting localized electric field appears within the metal substrate and there is hardly any interaction with the mirror image mode. This indicates that the lateral interaction can be adjusted by the gap distance between the metal nanostructures and the coupling with the FP mode and mirror image mode can also be controlled. This allows for the plasmon mode coupling to be freely adjusted according to the application and purpose. It suggests that the resonance peak wavelength and intensity can be flexibly tuned independently. Also, by controlling the ratio of both, it may be possible to control the degree of the dark mode and, consequently, the ratio of radiation to absorption from the LSPR. This could enable the control of optical properties tailored to the application, such as enhanced scattering, emission, light absorption, light harvesting, and improved sensor detection sensitivity.

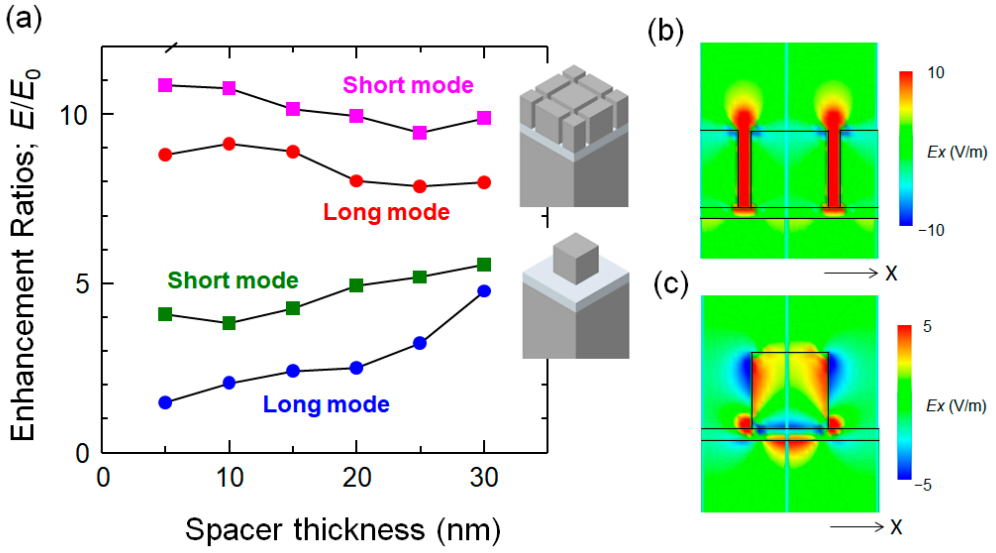

Figure 7. (**a**) Enhancement ratios for the electric field compared to the incident field for short and long modes with 30 nm Ag nanocubes/spacer/metal substrate models with Ag nanocubes alone and array structure with 5 nm gaps. X-polarized electric field distribution cross-sections for Ag nanocubes alone (**b**) and array structure with 5 nm gaps (**c**) on spacer/metal substrate models.

For imaging, nanostructures with nanodisks concentrated at contact points, rather than nanospheres with localized electric fields concentrated at a single point, and even nanocubes concentrated on the surfaces they touch, are beneficial for creating a uniform enhancement field over a wide area. When adjusting the resonance wavelength, the size and gap of the nanostructure are usually adjusted, but this change affects the region and penetration depth of the plasmon coupling and localized electric field. By using a two-dimensional nano-periodic structure combined with an MIM structure, it is possible to flexibly adjust only the resonance wavelength based on the dielectric thickness, while maintaining the size and gap of the nanostructure. In actual microscopic measurements, it is essential to tune the resonance conditions to match the excitation and fluorescence wavelengths. Bearing these points in mind, in this study, we designed and optimized nano-array structures of plasmonic metamaterials by simulation, but attempts to fabricate them and demonstrate control of their optical properties are currently in progress and will be reported at the next opportunity.

Our work on nanocube arrays has revealed important parameters such as nanogap size and spacer layer thickness that significantly affect optical properties via Fabry–Perot modes and mirror-image modes. These findings not only advance our understanding of plasmonic metamaterial behavior but also provide practical guidelines for designing next-generation devices. By fine-tuning these parameters, future research can leverage our findings to develop plasmonic devices with unparalleled sensitivity and resolution, thereby opening new avenues for high-sensitivity imaging applications. In addition to imaging, the ability to control plasmon coupling modes via Fabry–Perot modes and mirror-image modes holds potential for a variety of applications. For example, since the spectrum of optical absorption and scattering can be controlled, it is anticipated to lead to high-efficiency light-emitting devices and solar cells, and to low-threshold nano-lasers, by achieving high Q-values. Furthermore, it is poised to open the door to various applications such as optical entanglement and optical quantum devices based on the strong coupling of plasmon modes and highly integrated nano-optical circuits utilizing the extreme optical confinement properties.

4. Conclusions

Our investigation into the intricate domain of plasmonic metamaterials has yielded pivotal insights into the manipulation of light at the nanoscale. We have meticulously crafted and analyzed various nanostructural arrays, delving into their electric field interactions and the resulting plasmonic behaviors, providing insights that are crucial for the advancement of high-sensitivity imaging techniques. Our findings articulate the significant role of geometric configuration, particularly the gaps between nanostructures, in defining the strength and localization of electric fields, which are instrumental in enhancing optical responses for high-resolution imaging. By extensively analyzing the interactions within metal nanostructure/spacer/metal substrate constructs, we have revealed the intricate behaviors of electric field enhancements at different spacer layer thicknesses. Our findings reveal that the resonance peak wavelength and mode intensity are highly dependent on spacer thickness, which can be manipulated to fine-tune the optical responses of the nanostructures. Through FDTD simulations, we have demonstrated the capacity to predict and control the LSPRs by adjusting nanostructural dimensions. In summary, the strategic design and optimization of nanostructured arrays in plasmonic metamaterials represents a significant leap forward in the quest for sensitive and high-resolution imaging technologies. Our research not only demonstrates the feasibility of enhancing imaging capabilities through nanophotonics, but also highlights the endless possibilities that lie at the intersection of material science, optics, and nanotechnology. As we continue to explore this fascinating domain, the prospects for new applications and technologies that leverage the unique advantages of plasmonic metamaterials are boundless, promising to usher in a new era of scientific exploration and technological innovation.

Author Contributions: Conceptualization, methodology, K.O. and K.T.; software, K.O. and D.T.; validation, T.M., K.W. and Y.A.; investigation, resources, data curation, writing, K.O.; project administration and funding acquisition, K.O. and K.T. All authors have read and agreed to the published version of the manuscript.

Funding: This work was supported by the JSPS Grants-in-Aid for Scientific Research (S) (No. JP19H05627) and Specially Promoted Research (No. JP20H05622).

Institutional Review Board Statement: Not applicable.

Informed Consent Statement: Not applicable.

Data Availability Statement: The data presented in this study are available on request from the corresponding author.

Conflicts of Interest: The funders had no role in the design of the study; in the collection, analyses, or interpretation of data; in the writing of the manuscript; or in the decision to publish the results.

References

1. Yao, K.; Liu, Y. Plasmonic metamaterials. *Nanotechnol. Rev.* **2014**, *3*, 177–210. [CrossRef]
2. Tang, S.; He, Q.; Xiao, S.; Huang, X.; Zhou, L. Fractal plasmonic metamaterials: Physics and applications. *Nanotechnol. Rev.* **2015**, *4*, 277–288. [CrossRef]
3. Hess, O.; Pendry, J.B.; Maier, S.A.; Oulton, R.F.; Hamm, J.M.; Tsakmakidis, K.L. Active nanoplasmonic metamaterials. *Nat. Mater.* **2012**, *11*, 573–584. [CrossRef]
4. Cui, Y.; He, Y.; Jin, Y.; Ding, F.; Yang, L.; Ye, Y.; Zhong, S.; Lin, Y.; He, S. Plasmonic and metamaterial structures as electromagnetic absorbers. *Laser Photonics Rev.* **2014**, *8*, 495–520. [CrossRef]
5. Shin, H.; Fan, S. All-angle negative refraction for surface plasmon waves using a metal-dielectric-metal structure. *Phys. Rev. Lett.* **2006**, *96*, 073907. [CrossRef]
6. Xu, T.; Agrawal, A.; Abashin, M.; Chau, K.J.; Lezec, H.J. All-angle negative refraction and active flat lensing of ultraviolet light. *Nature* **2013**, *497*, 470–474. [CrossRef]
7. Su, D.; Zhang, X.-Y.; Ma, Y.-L.; Shan, F.; Wu, J.-Y.; Fu, X.-C.; Zhang, L.-J.; Yuan, K.-Q.; Zhang, T. Real-Time Electro-Optical Tunable Hyperlens under Subwavelength Scale. *IEEE Photonics J.* **2018**, *10*, 1–9. [CrossRef]
8. Luo, X. Subwavelength Artificial Structures: Opening a New Era for Engineering Optics. *Adv. Mater.* **2019**, *31*, e18046802019. [CrossRef]

9. Cheng, B.H.; Ho, Y.Z.; Lan, Y.C.; Tsai, D.P. Optical Hybrid-Superlens Hyperlens for Superresolution Imaging. *IEEE J. Sel. Top. Quantum Electron.* **2013**, *19*, 4601305. [CrossRef]
10. Silveirinha, M.G.; Alu, A.; Engheta, N. Parallel-plate metamaterials for cloaking structures. *Phys. Rev. E Stat. Nonlinear Soft Matter Phys.* **2007**, *75*, 036603. [CrossRef]
11. Monticone, F.; Alù, A. Metamaterials and plasmonics: From nanoparticles to nanoantenna arrays, metasurfaces, and metamaterials. *Chin. Phys. B* **2014**, *23*, 047809. [CrossRef]
12. Alù, A.; Engheta, N. Cloaking a receiving antenna or a sensor with plasmonic metamaterials. *Metamaterials* **2010**, *4*, 153–159. [CrossRef]
13. Ogawa, S.; Kimata, M. Metal-Insulator-Metal-Based Plasmonic Metamaterial Absorbers at Visible and Infrared Wavelengths: A Review. *Materials* **2018**, *11*, 458. [CrossRef]
14. Li, J.; Gan, R.; Guo, Q.; Liu, H.; Xu, J.; Yi, F. Tailoring optical responses of infrared plasmonic metamaterial absorbers by optical phonons. *Opt. Express* **2018**, *26*, 16769–16781. [CrossRef]
15. Lai, G.; Liang, R.; Zhang, Y.; Bian, Z.; Yi, L.; Zhan, G.; Zhao, R. Double plasmonic nanodisks design for electromagnetically induced transparency and slow light. *Opt. Express* **2015**, *23*, 6554–6561. [CrossRef]
16. Bai, Z.; Huang, G.; Liu, L.; Zhang, S. Giant Kerr nonlinearity and low-power gigahertz solitons via plasmon-induced transparency. *Sci. Rep.* **2015**, *5*, 13780. [CrossRef]
17. Pang, S.; Huo, Y.; Xie, Y.; Hao, L. Fano resonance in MIM waveguide structure with oblique rectangular cavity and its application in sensor. *Opt. Commun.* **2016**, *381*, 409–413. [CrossRef]
18. Huang, W.; Xu, R.; Lin, Y.-S.; Chen, C.-H. Three-dimensional pyramid metamaterial with tunable broad absorption bandwidth. *AIP Adv.* **2020**, *10*, 035125. [CrossRef]
19. Chorsi, H.T.; Lee, Y.; Alu, A.; Zhang, J.X.J. Tunable plasmonic substrates with ultrahigh Q-factor resonances. *Sci. Rep.* **2017**, *7*, 15985. [CrossRef]
20. Luo, X.; Pu, M.; Guo, Y.; Li, X.; Zhang, F.; Ma, X. Catenary Functions Meet Electromagnetic Waves: Opportunities and Promises. *Adv. Opt. Mater.* **2020**, *8*, 2001194. [CrossRef]
21. Ma, C. Designing super-resolution metalenses by the combination of metamaterials and nanoscale plasmonic waveguide couplers. *J. Nanophotonics* **2011**, *5*, 051604. [CrossRef]
22. Ogawa, S.; Kimata, M. Wavelength- or Polarization-Selective Thermal Infrared Detectors for Multi-Color or Polarimetric Imaging Using Plasmonics and Metamaterials. *Materials* **2017**, *10*, 493. [CrossRef]
23. Wan, W.; Gao, J.; Yang, X. Metasurface Holograms for Holographic Imaging. *Adv. Opt. Mater.* **2017**, *5*, 1700541. [CrossRef]
24. Nagasaki, Y.; Hotta, I.; Suzuki, M.; Takahara, J. Metal-Masked Mie-Resonant Full-Color Printing for Achieving Free-Space Resolution Limit. *ACS Photonics* **2018**, *5*, 3849–3855. [CrossRef]
25. Mudachathi, R.; Tanaka, T. Up Scalable Full Colour Plasmonic Pixels with Controllable Hue, Brightness and Saturation. *Sci. Rep.* **2017**, *7*, 1199. [CrossRef]
26. Cheng, F.; Gao, J.; Stan, L.; Rosenmann, D.; Czaplewski, D.; Yang, X. Aluminum plasmonic metamaterials for structural color printing. *Opt. Express* **2015**, *23*, 14552–14560. [CrossRef]
27. Cheng, F.; Yang, X.; Rosenmann, D.; Stan, L.; Czaplewski, D.; Gao, J. Enhanced structural color generation in aluminum metamaterials coated with a thin polymer layer. *Opt. Express* **2015**, *23*, 25329–25339. [CrossRef]
28. Deshpande, R.A.; Roberts, A.S.; Bozhevolnyi, S.I. Plasmonic color printing based on third-order gap surface plasmons [Invited]. *Opt. Mater. Express* **2019**, *9*, 717. [CrossRef]
29. Keshavarz Hedayati, M.; Elbahri, M. Review of Metasurface Plasmonic Structural Color. *Plasmonics* **2016**, *12*, 1463–1479. [CrossRef]
30. Wang, J.; Xu, Z.; Kotsifaki, D.G. Plasmonic and metamaterial biosensors: A game-changer for virus detection. *Sens. Diagn.* **2023**, *2*, 600–619. [CrossRef]
31. Wang, Z.; Chen, J.; Khan, S.A.; Li, F.; Shen, J.; Duan, Q.; Liu, X.; Zhu, J. Plasmonic Metasurfaces for Medical Diagnosis Applications: A Review. *Sensors* **2021**, *22*, 133. [CrossRef]
32. Kabashin, A.V.; Evans, P.; Pastkovsky, S.; Hendren, W.; Wurtz, G.A.; Atkinson, R.; Pollard, R.; Podolskiy, V.A.; Zayats, A.V. Plasmonic nanorod metamaterials for biosensing. *Nat. Mater.* **2009**, *8*, 867–871. [CrossRef]
33. Kravets, V.G.; Schedin, F.; Jalil, R.; Britnell, L.; Gorbachev, R.V.; Ansell, D.; Thackray, B.; Novoselov, K.S.; Geim, A.K.; Kabashin, A.V.; et al. Singular phase nano-optics in plasmonic metamaterials for label-free single-molecule detection. *Nat. Mater.* **2013**, *12*, 304–309. [CrossRef]
34. Politano, G.G.; Cazzanelli, E.; Versace, C.; Vena, C.; De Santo, M.P.; Castriota, M.; Ciuchi, F.; Bartolino, R. Graphene oxide on magnetron sputtered silver thin films for SERS and metamaterial applications. *Appl. Surf. Sci.* **2018**, *427*, 927–933. [CrossRef]
35. Wang, K.; Qiu, Z.; Qin, Y.; Feng, L.; Huang, L.; Xiao, G. Preparation and SERS performance of silver nanowires arrays on paper by automatic writing method. *Spectrochim. Acta A Mol. Biomol. Spectrosc.* **2022**, *281*, 121580. [CrossRef]
36. Borchers, A.; Pieler, T. Programming pluripotent precursor cells derived from Xenopus embryos to generate specific tissues and organs. *Genes* **2010**, *1*, 413–426. [CrossRef]
37. Sayed, S.I.; Mahmoud, K.R.; Mubarak, R.I. Design and optimization of broadband metamaterial absorber based on manganese for visible applications. *Sci. Rep.* **2023**, *13*, 11937. [CrossRef]

38. Ji, W.; Chang, J.; Xu, H.X.; Gao, J.R.; Groblacher, S.; Urbach, H.P.; Adam, A.J.L. Recent advances in metasurface design and quantum optics applications with machine learning, physics-informed neural networks, and topology optimization methods. *Light Sci. Appl.* **2023**, *12*, 169. [CrossRef]
39. Lan, G.; Wang, Y.; Ou, J.Y. Optimization of metamaterials and metamaterial-microcavity based on deep neural networks. *Nanoscale Adv.* **2022**, *4*, 5137–5143. [CrossRef]
40. Okamoto, K.; Lin, B.; Imazu, K.; Yoshida, A.; Toma, K.; Toma, M.; Tamada, K. Tuning Colors of Silver Nanoparticle Sheets by Multilayered Crystalline Structures on Metal Substrates. *Plasmonics* **2012**, *8*, 581–590. [CrossRef]
41. Okamoto, K.; Tanaka, D.; Degawa, R.; Li, X.; Wang, P.; Ryuzaki, S.; Tamada, K. Electromagnetically induced transparency of a plasmonic metamaterial light absorber based on multilayered metallic nanoparticle sheets. *Sci. Rep.* **2016**, *6*, 36165. [CrossRef]
42. Shinohara, S.; Tanaka, D.; Okamoto, K.; Tamada, K. Colorimetric plasmon sensors with multilayered metallic nanoparticle sheets. *Phys. Chem. Chem. Phys.* **2015**, *17*, 18606–18612. [CrossRef]
43. Degawa, R.; Wang, P.; Tanaka, D.; Park, S.; Sakai, N.; Tatsuma, T.; Okamoto, K.; Tamada, K. Colorimetric Detection of an Airborne Remote Photocatalytic Reaction Using a Stratified Ag Nanoparticle Sheet. *Langmuir* **2016**, *32*, 8154–8162. [CrossRef]
44. Ishijima, A.; Wang, P.; Ryuzaki, S.; Okamoto, K.; Tamada, K. Comparison of LSPR-mediated enhanced fluorescence excited by S- and P-polarized light on a two-dimensionally assembled silver nanoparticle sheet. *Appl. Phys. Lett.* **2018**, *113*, 171602. [CrossRef]
45. Masuda, S.; Yanase, Y.; Usukura, E.; Ryuzaki, S.; Wang, P.P.; Okamoto, K.; Kuboki, T.; Kidoaki, S.; Tamada, K. High-resolution imaging of a cellattached nanointerface using a gold-nanoparticle two-dimensional sheet. *Sci. Rep.* **2017**, *7*, 3720. [CrossRef]
46. Calandrini, E.; Cerea, A.; De Angelis, F.; Zaccaria, R.P.; Toma, A. Magnetic hot-spot generation at optical frequencies: From plasmonic metamolecules to all-dielectric nanoclusters. *Nanophotonics* **2018**, *8*, 45–62. [CrossRef]
47. Su, D.S.; Tsai, D.P.; Yen, T.J.; Tanaka, T. Ultrasensitive and Selective Gas Sensor Based on a Channel Plasmonic Structure with an Enormous Hot Spot Region. *ACS Sens.* **2019**, *4*, 2900–2907. [CrossRef]
48. Wy, Y.; Jung, H.; Hong, J.W.; Han, S.W. Exploiting Plasmonic Hot Spots in Au-Based Nanostructures for Sensing and Photocatalysis. *Acc. Chem. Res.* **2022**, *55*, 831–843. [CrossRef]
49. Johnson, P.B.; Christy, R.W. Optical Constants of the Noble Metals. *Phys. Rev. B* **1972**, *6*, 4370–4379. [CrossRef]
50. Bishop, K.J.; Wilmer, C.E.; Soh, S.; Grzybowski, B.A. Nanoscale forces and their uses in self-assembly. *Small* **2009**, *5*, 1600–1630. [CrossRef]
51. Cheng, S.-C.; Wen, T.-C. Robust SERS substrates with massive nanogaps derived from silver nanocubes self-assembled on massed silver mirror via 1,2-ethanedithiol monolayer as linkage and ultra-thin spacer. *Mater. Chem. Phys.* **2014**, *143*, 1331–1337. [CrossRef]
52. Fan, J.A.; Wu, C.H.; Bao, K.; Bao, J.M.; Bardhan, R.; Halas, N.J.; Manoharan, V.N.; Nordlander, P.; Shvets, G.; Capasso, F. Self-Assembled Plasmonic Nanoparticle Clusters. *Science* **2010**, *328*, 1135–1138. [CrossRef]
53. Gong, J.; Li, G.; Tang, Z. Self-assembly of noble metal nanocrystals: Fabrication, optical property, and application. *Nano Today* **2012**, *7*, 564–585. [CrossRef]
54. Hanske, C.; Tebbe, M.; Kuttner, C.; Bieber, V.; Tsukruk, V.V.; Chanana, M.; Konig, T.A.; Fery, A. Strongly coupled plasmonic modes on macroscopic areas via template-assisted colloidal self-assembly. *Nano Lett.* **2014**, *14*, 6863–6871. [CrossRef]
55. Rozin, M.J.; Rosen, D.A.; Dill, T.J.; Tao, A.R. Colloidal metasurfaces displaying near-ideal and tunable light absorbance in the infrared. *Nat. Commun.* **2015**, *6*, 7325. [CrossRef]
56. Wang, Y.; Zheng, Y.; Huang, C.Z.; Xia, Y. Synthesis of Ag nanocubes 18-32 nm in edge length: The effects of polyol on reduction kinetics, size control, and reproducibility. *J. Am. Chem. Soc.* **2013**, *135*, 1941–1951. [CrossRef]
57. Zhang, Q.; Li, W.; Wen, L.P.; Chen, J.; Xia, Y. Facile synthesis of Ag nanocubes of 30 to 70 nm in edge length with CF(3)COOAg as a precursor. *Chemistry* **2010**, *16*, 10234–10239. [CrossRef]
58. Zhou, S.; Li, J.; Gilroy, K.D.; Tao, J.; Zhu, C.; Yang, X.; Sun, X.; Xia, Y. Facile Synthesis of Silver Nanocubes with Sharp Corners and Edges in an Aqueous Solution. *ACS Nano* **2016**, *10*, 9861–9870. [CrossRef]
59. Mitomo, H.; Takeuchi, C.; Sugiyama, R.; Tamada, K.; Ijiro, K. Thermo-Responsive Silver Nanocube Assembled Films. *Bull. Chem. Soc. Jpn.* **2022**, *95*, 771–773. [CrossRef]
60. Okamoto, K.; Okura, K.; Wang, P.; Ryuzaki, S.; Tamada, K. Flexibly tunable surface plasmon resonance by strong mode coupling using a random metal nanohemisphere on mirror. *Nanophotonics* **2020**, *9*, 3409–3418. [CrossRef]
61. Shimanoe, K.; Endo, S.; Matsuyama, T.; Wada, K.; Okamoto, K. Localized surface plasmon resonance in deep ultraviolet region below 200 nm using a nanohemisphere on mirror structure. *Sci. Rep.* **2021**, *11*, 5169. [CrossRef]
62. Shimanoe, K.; Endo, S.; Matsuyama, T.; Wada, K.; Okamoto, K. Metallic nanovoid and nano hemisphere structures fabricated via simple methods to control localized surface plasmon resonances in UV and near IR wavelength regions. *Appl. Phys. Express* **2021**, *14*, 042007. [CrossRef]
63. Wan, M.; Zhai, W.; Song, Y.; Li, Y.; Ji, P.; Zhou, F. Actively controllable EIT-like resonance between localized and propagating surface plasmons for optical switching. *J. Mod. Opt.* **2015**, *62*, 1264–1269. [CrossRef]
64. Yang, J.; Sun, Q.; Ueno, K.; Shi, X.; Oshikiri, T.; Misawa, H.; Gong, Q. Manipulation of the dephasing time by strong coupling between localized and propagating surface plasmon modes. *Nat. Commun.* **2018**, *9*, 4858. [CrossRef]
65. Huang, Y.; Ma, L.; Li, J.; Zhang, Z. Nanoparticle-on-mirror cavity modes for huge and/or tunable plasmonic field enhancement. *Nanotechnology* **2017**, *28*, 105203. [CrossRef]

66. Zhang, C.; Hugonin, J.-P.; Greffet, J.-J.; Sauvan, C. Surface Plasmon Polaritons Emission with Nanopatch Antennas: Enhancement by Means of Mode Hybridization. *ACS Photonics* **2019**, *6*, 2788–2796. [CrossRef]
67. Shi, X.; Ueno, K.; Oshikiri, T.; Sun, Q.; Sasaki, K.; Misawa, H. Enhanced water splitting under modal strong coupling conditions. *Nat. Nanotechnol.* **2018**, *13*, 953–958. [CrossRef]